Science Advances

AAAS

advances.sciencemag.org/cgi/content/full/2/11/e1601185/DC1

Supplementary Materials for

Epidermal mechano-acoustic sensing electronics for cardiovascular diagnostics and human-machine interfaces

Yuhao Liu, James J. S. Norton, Raza Qazi, Zhanan Zou, Kaitlyn R. Ammann, Hank Liu, Lingqing Yan, Phat L. Tran, Kyung-In Jang, Jung Woo Lee, Douglas Zhang, Kristopher A. Kilian, Sung Hee Jung, Timothy Bretl, Jianliang Xiao, Marvin J. Slepian, Yonggang Huang, Jae-Woong Jeong, John A. Rogers

Published 16 November 2016, *Sci. Adv.* **2**, e1601185 (2016)
DOI: 10.1126/sciadv.1601185

The PDF file includes:

- fig. S14. Acoustic signals from aortic, pulmonary, tricuspid, and mitral sites of a patient with irregular heartbeat.
- fig. S15. Experiment on LVAD pump thrombosis.
- fig. S16. Data captured using a reported device and a commercial microphone in quiet and noisy environments.
- fig. S17. Process loop for a speech-based human-machine interface.
- fig. S18. Demonstration of noise reduction in time domain speech data.
- fig. S19. Authentication application.
- fig. S20. Wireless sensing of BioStamp.
- Legends for movies S1 to S3

Other Supplementary Material for this manuscript includes the following:
(available at advances.sciencemag.org/cgi/content/full/2/11/e1601185/DC1)

- movie S1 (.avi and .mp4 format). Movie of speech recording in a quiet environment.
- movie S2 (.avi and .mp4 format). Movie of speech recording in a noisy environment.
- movie S3 (.avi and wmv format). Movie of speech recognition and voice control of a Pac-Man game with real-time machine learning and signal classification.

Supplementary Note

note S1. Analytical model for mass effect on acceleration.

Since the vibration tests involve a rigid platform and a thin (0.3 mm) layer of Ecoflex between the sensor and the platform, effects of damping can be ignored. The system can thus be described by

$$m\ddot{x} + kx = F \tag{1}$$

where m is the total mass, k is the stiffness of the vibration generator and F is the force applied on the system. The applied force takes the form of a square wave, according to

$$F = A\left\{2\left[H\left(\frac{t}{T}\right) - H\left(\frac{t}{T} - 1\right)\right] - 1\right\} \tag{2}$$

where A is a constant related to the amplitude of the force, $H(t/T) = \begin{cases} 0, & \text{t} < 0 \\ 1, & \text{t} \geq 0 \end{cases}$ is Heaviside step function, and T is the half period of the square wave. By Fourier analysis, the force function can be written as

$$F = A\frac{4}{\pi}\sum_{n=1,3,5}^{\infty}\frac{1}{n}\sin\left(\frac{n\pi t}{T}\right) \tag{3}$$

By combining Eqs. (1) and (3), the solution can be obtained as

$$x = 4A\sum_{n=1,3,5}^{\infty}\frac{1}{n\pi\left[k - m\left(n\pi/T\right)^2\right]}\sin\left(\frac{n\pi t}{T}\right) \tag{4}$$

And the acceleration is

$$\ddot{x} = -4A\sum_{n=1,3,5}^{\infty}\frac{n\pi}{n\pi\left[kT^2 - m\left(n\pi\right)^2\right]}\sin\left(\frac{n\pi t}{T}\right) \tag{5}$$

The acceleration times the sensitivity of the accelerometer (0.3V/g) gives the corresponding voltage measured in experiment.

note S2. Effect of low-modulus device substrate.

To demonstrate the advantages of soft epidermal electronics over conventional rigid devices, an idealized 2D vibration model was established using commercial finite element software ABAQUS. A schematic illustration of this model is in fig. S11. The accelerometer (red box) of mass 213.6 mg was placed at the middle of the device substrate, and the mass object (yellow box) of mass 6.8 g was placed either at the middle, on the left or on the right. Two types of substrate with different stiffnesses were studied to demonstrate the key effects. One substrate was made of relatively rigid acrylic plate, with Young's modulus 3.1 GPa, thickness 5 mm and mass 9.39 g. The other substrate was made of Ecoflex, with Young's modulus 69 kPa, thickness 5 mm and mass 7.8 g. The width of the substrate was 40 mm, and the size of the mass and accelerometer were assumed to be 5 mm by 5 mm. Force input was assumed to take the form of a sine function as the excitation, with a frequency 100 Hz. Modal dynamic method and frequency analysis were combined to simulate the system vibration. The substrate, mass objects and the accelerometer were modeled by 2D planner element CPE4R. Four cases were investigated: without the mass object, and with the mass object on top of the accelerometer, on the left edge, and on the right edge of the substrate. From the simulation results, when there is no mass object, the acceleration detected by the accelerometer is similar for both hard and soft substrates. When mass objects are introduced to the hard substrate, the acceleration amplitude decreases significantly, without sensitivity to the location of these objects. However, for soft substrate, placing the mass on top of the accelerometer significantly decreases the acceleration detected by the accelerometer, but placing it elsewhere has negligible effect. Here, the soft substrate decouples mechanical loading at one location from mechanical vibration at another location.

Supplementary Figures

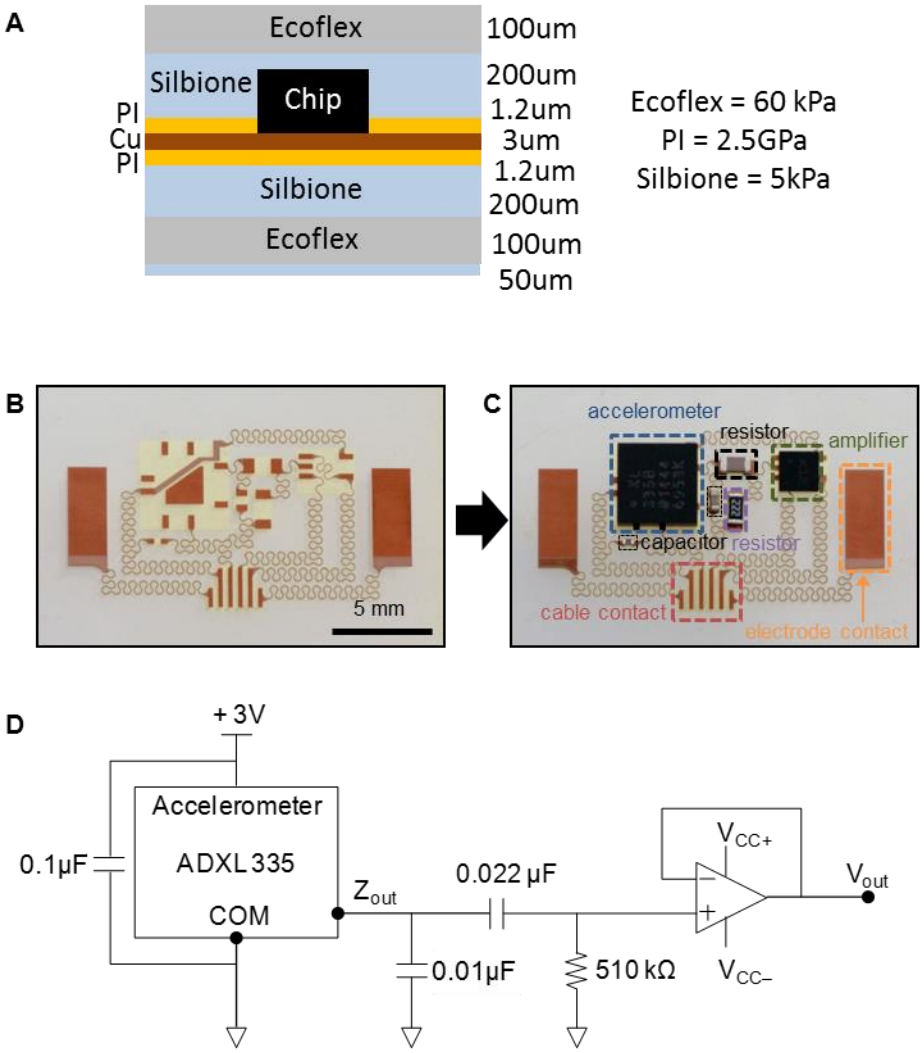

fig. S1. Device design and circuit layouts. (**A**) Cross sectional schematic illustration with thickness and modulus information. (**B**) Circuit layout of the device before and after chip bonding. (**C**) Equivalent circuit diagram.

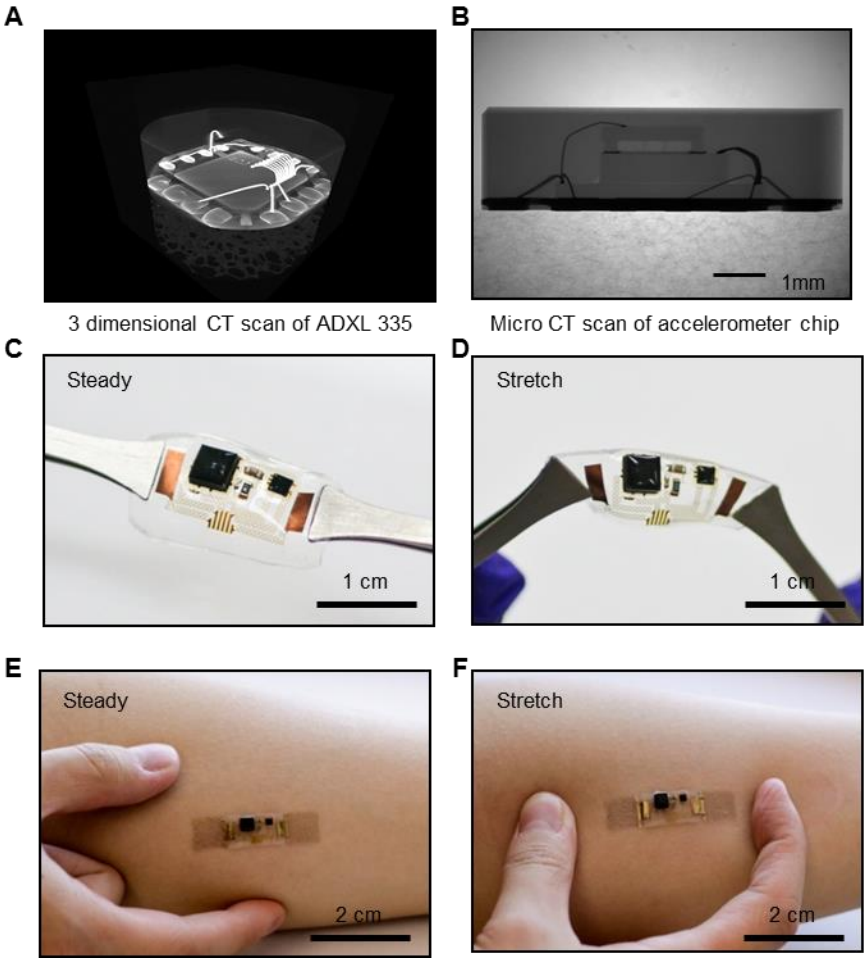

fig. S2. Computed x-ray tomography images of the internal structures of the accelerometer chip. (**A**) 3-dimensional Micro-CT image viewed from the top. (**B**) Micro-CT image viewed from the side.

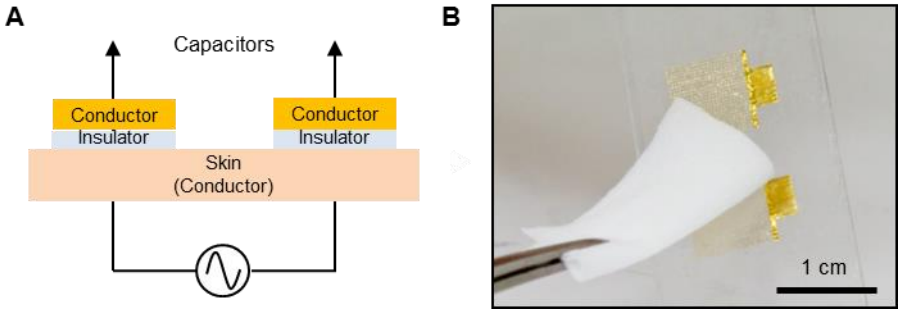

fig. S3. Schematic illustration of capacitive ECG electrodes and demonstrations of their reusability. (**A**) Structural layout of a capacitive electrode on skin during sensing. (**B**) Alcohol prep wipes can be used to clean the electrodes for repetitive use.

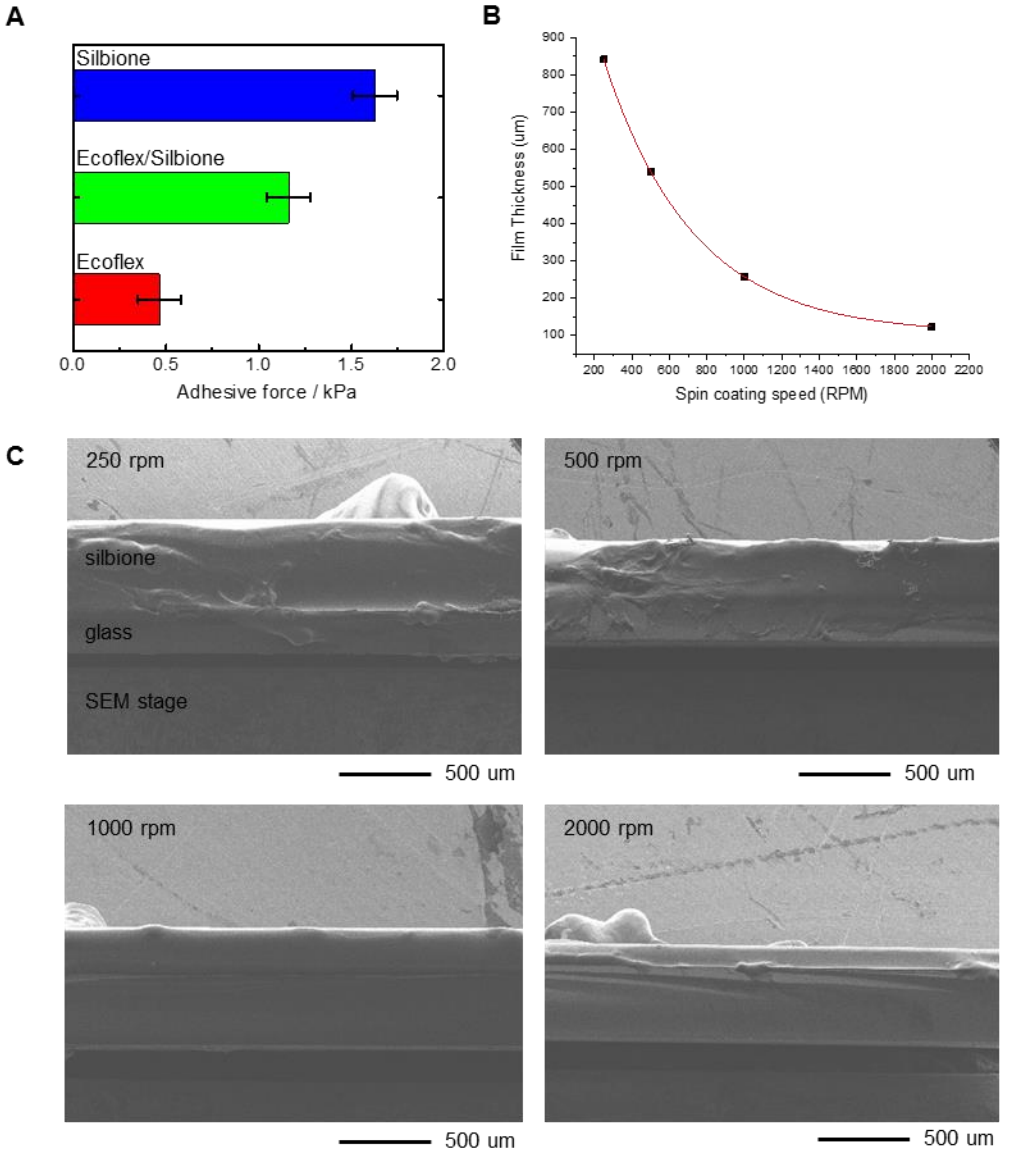

D

Spin coating speed (rpm)	250	500	1000	2000
Thickness (um)	841 ± 10	540 ± 10	258 ± 10	123 ± 10

fig. S4. Adhesion strength of Silbione to the skin and dependence of its thickness on spin speed. (**A**) Silicone-skin adhesion test results. (**B**) Film thickness as a function of spin-coating speed with fitted curve. (**C**) Scanning electron micrographs of the cross-sections of measured samples. (**D**) The table shows the measured film thicknesses at corresponding spin coating speeds.

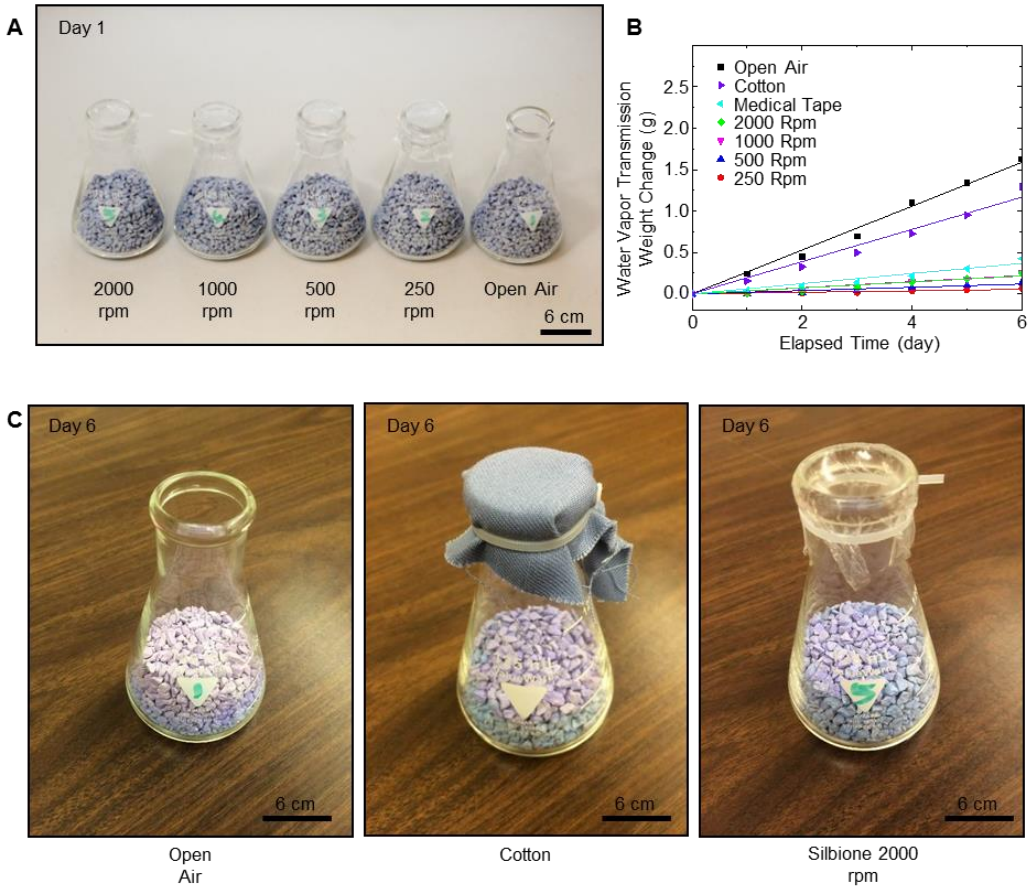

D

	Open Air	250	500	1000	2000	Medical	Cotton
Slope (g/day)	0.265	0.009	0.020	0.037	0.037	0.062	0.195
Slope (g/h)	0.011	0.000	0.001	0.002	0.002	0.003	0.008
TEWL	21.26	0.74	1.59	2.97	3.00	4.94	15.63

TEWL: Transmission Water-Vapor Loss

fig. S5. Measurements of water vapor transmission loss. (**A**) Experimental set-up. (**B**) Calculated water-vapor transmission weight change for films of Silbione. (**C**) Results of the experiment on Day 6. (**D**) Table for the calculation of water-vapor transmission loss on all films.

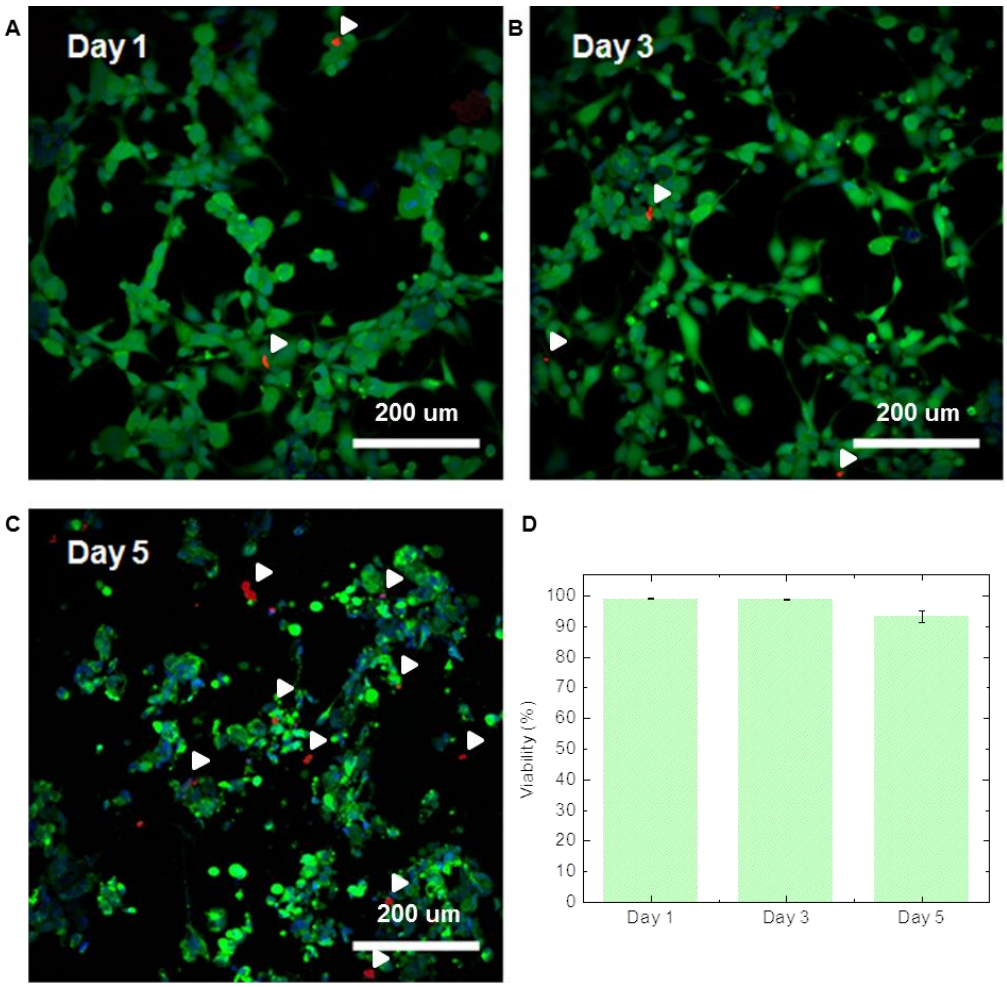

fig. S6. Cell viability assay and cytotoxicity test. (**A**) Immunofluorescent images of the device on Day 1, (**B**) Day 3, and (**C**) Day 5. (**D**) Results of cell viability assay.

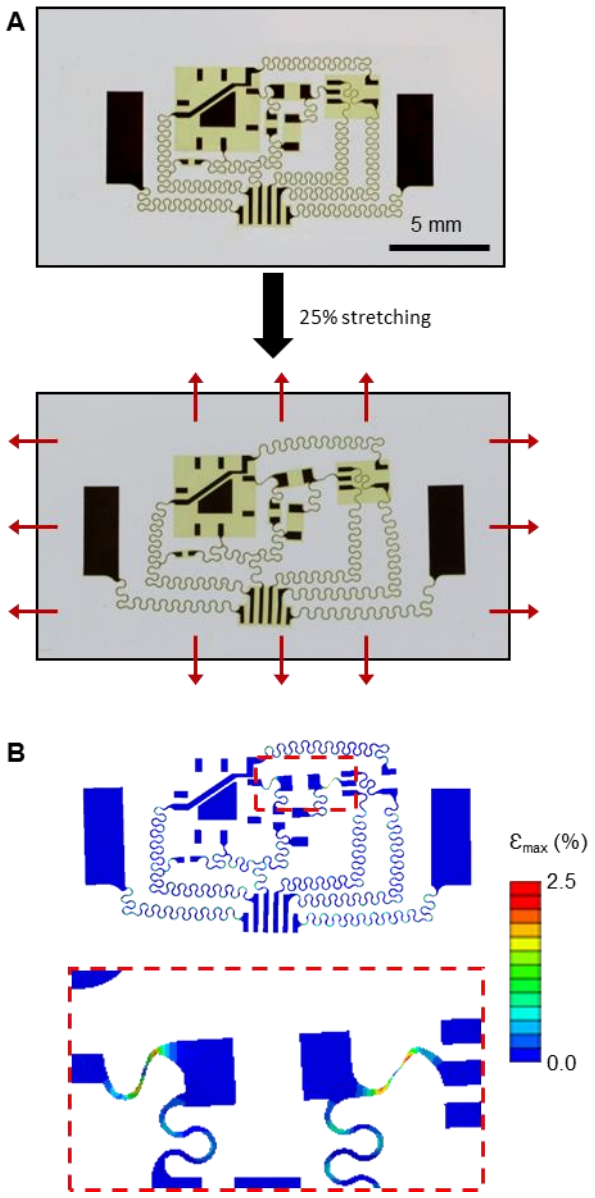

fig. S7. Mechanical simulation of the circuit interconnects during biaxial stretching. (**A**) Optical images of circuit interconnect under pre-stretching and bi-axial 25% stretching. (**B**) Mechanical simulation results with an enlarged image of the structures that experience the largest strain.

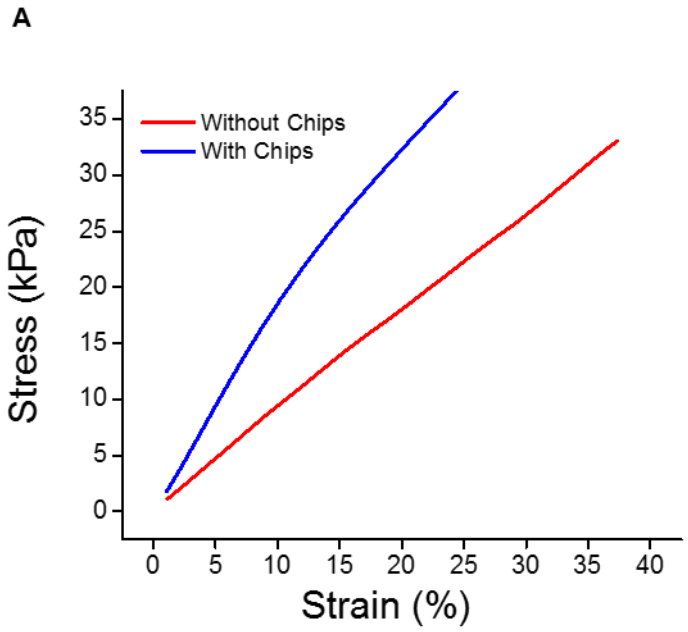

fig. S8. Stress-strain response of the device. (**A**) Dynamic mechanical analysis of the device with and without commercial chips bonded.

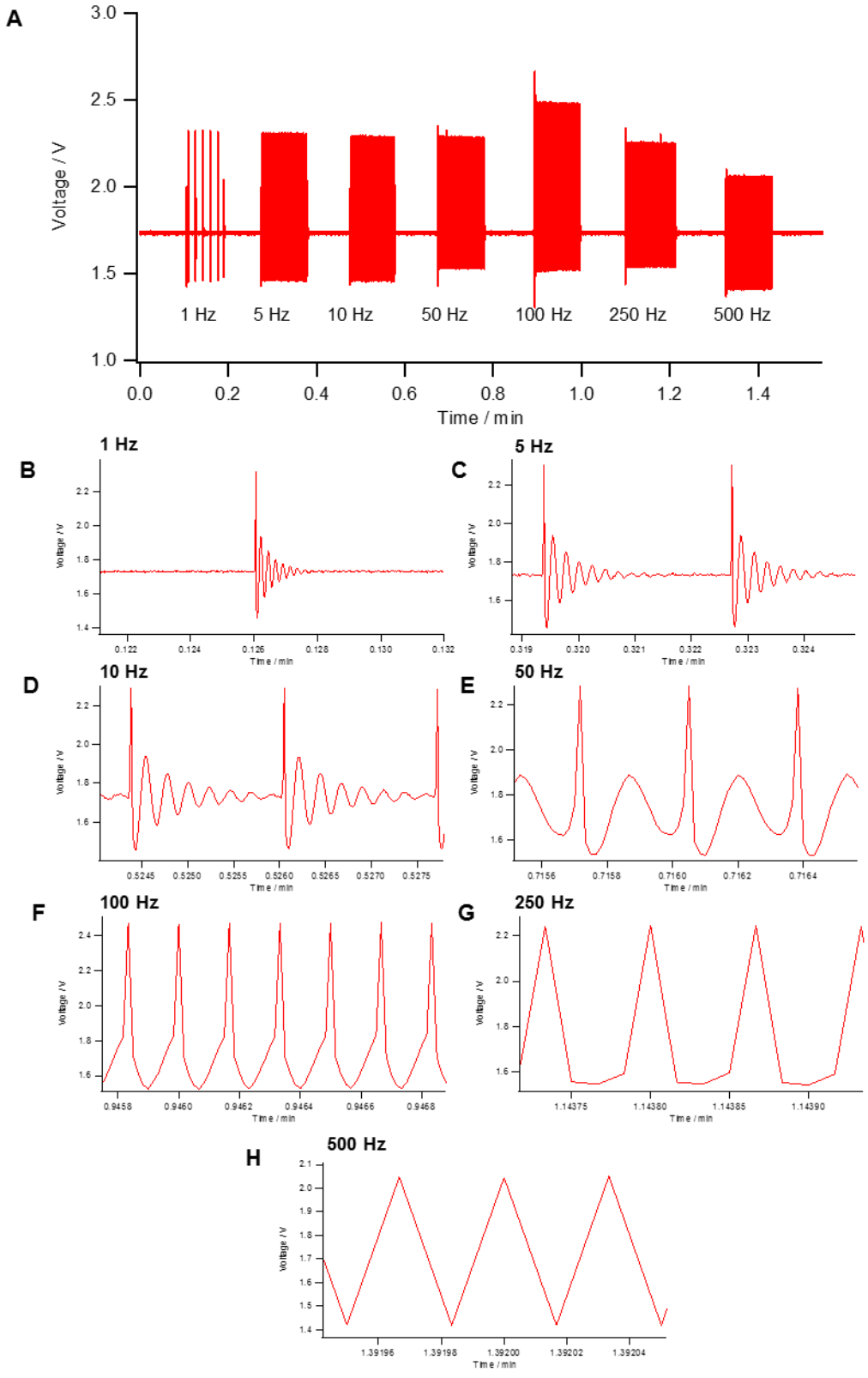

fig. S9. Vibration response of the accelerometer chip without analog filters. (**A**) Vibration response with time interval between discrete testing frequencies. Vibration response at (**B**) 1 Hz, (**C**) 5 Hz, (**D**) 10 Hz, (**E**) 50 Hz, (**F**) 100 Hz, (**G**) 250 Hz, (**H**) 500 Hz.

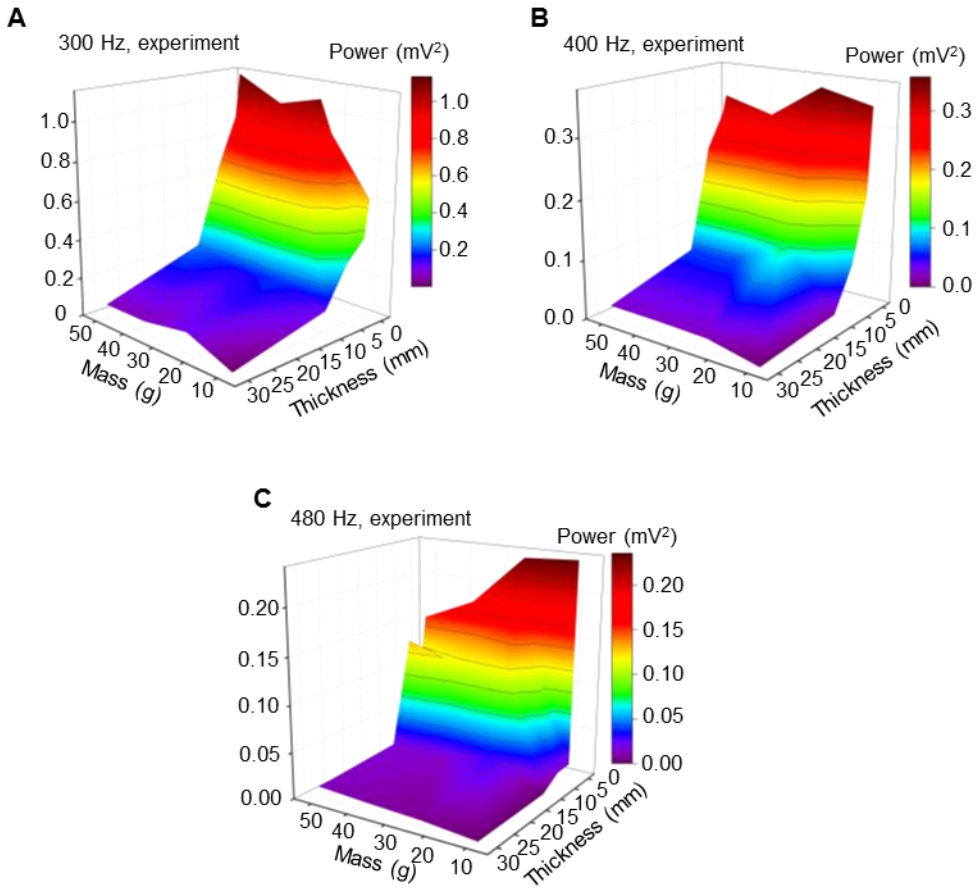

fig. S10. Comparison of experimental and simulation results on the effect of mass, tissue thickness, and signal frequency on measurement response. Spectral power distribution as a function of mass and tissue thickness at (**A**) 300 Hz, (**B**) 400 Hz, (**C**) 480 Hz.

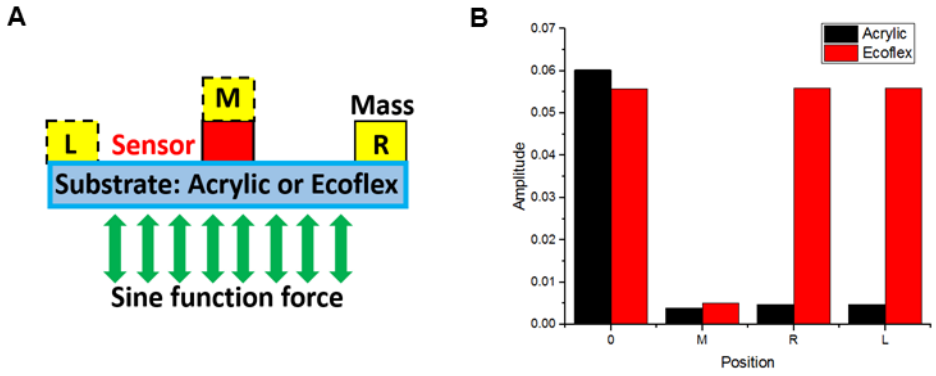

fig. S11. Schematic illustration and measurement results of the vibration model to capture the effects of device modulus. (**A**) Schematic illustration of the simulation setup. (**B**) Simulation results at three mass locations; 0 corresponds to the case of zero added mass.

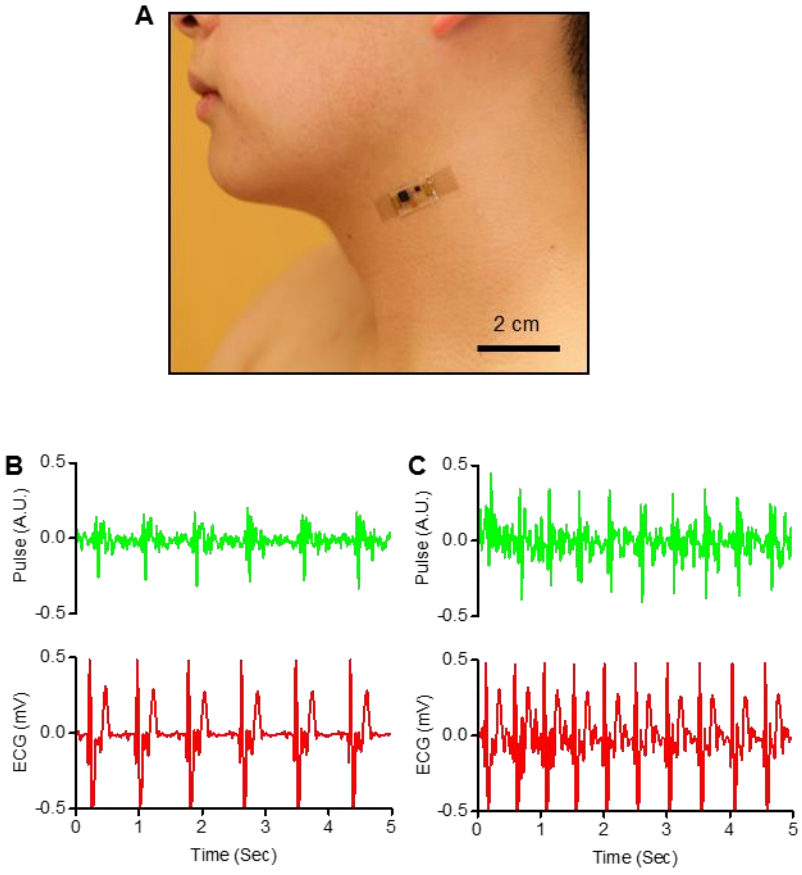

fig. S12. Application of an epidermal mechano-acoustic–electrophysiological device on the neck. (**A**) Optical images of sensor placed over the carotid artery. (**B**) Simultaneous measurement of ECG and pulse signal during rest. (**C**) Simultaneous measurement of ECG and pulse signal after exercise.

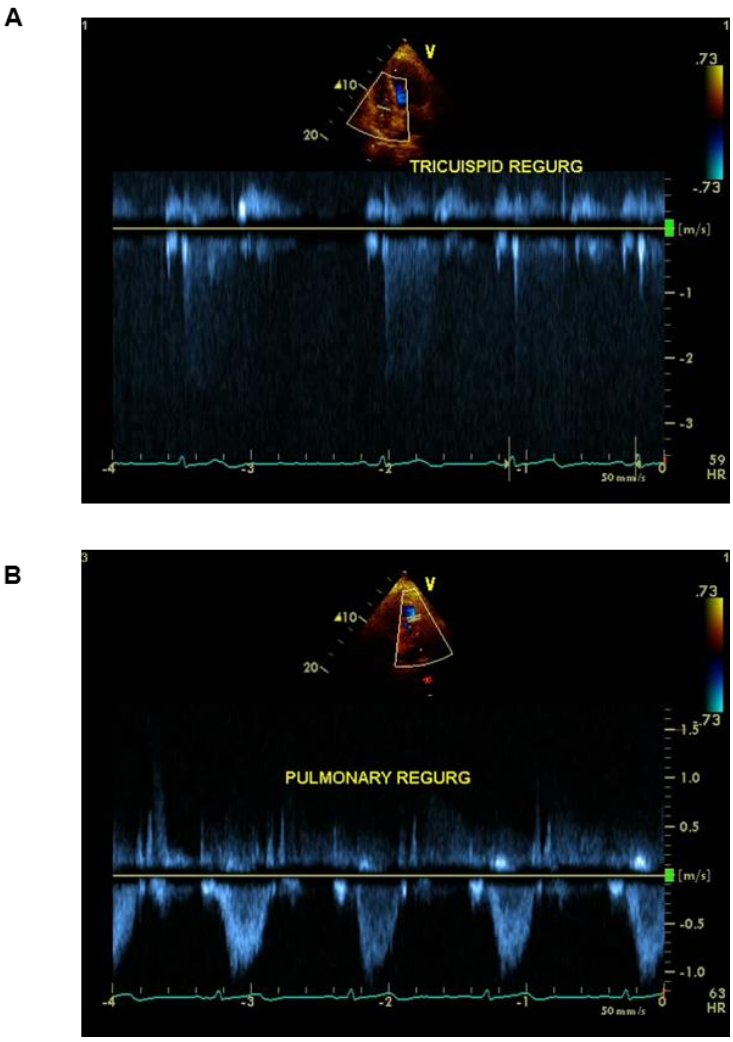

fig. S13. Echocardiogram characterization results on a patient with tricuspid and pulmonary regurgitation. (**A**) Echocardiography in the top and ECG at the bottom for tricuspid valve measurement, and (**B**) pulmonary valve measurement.

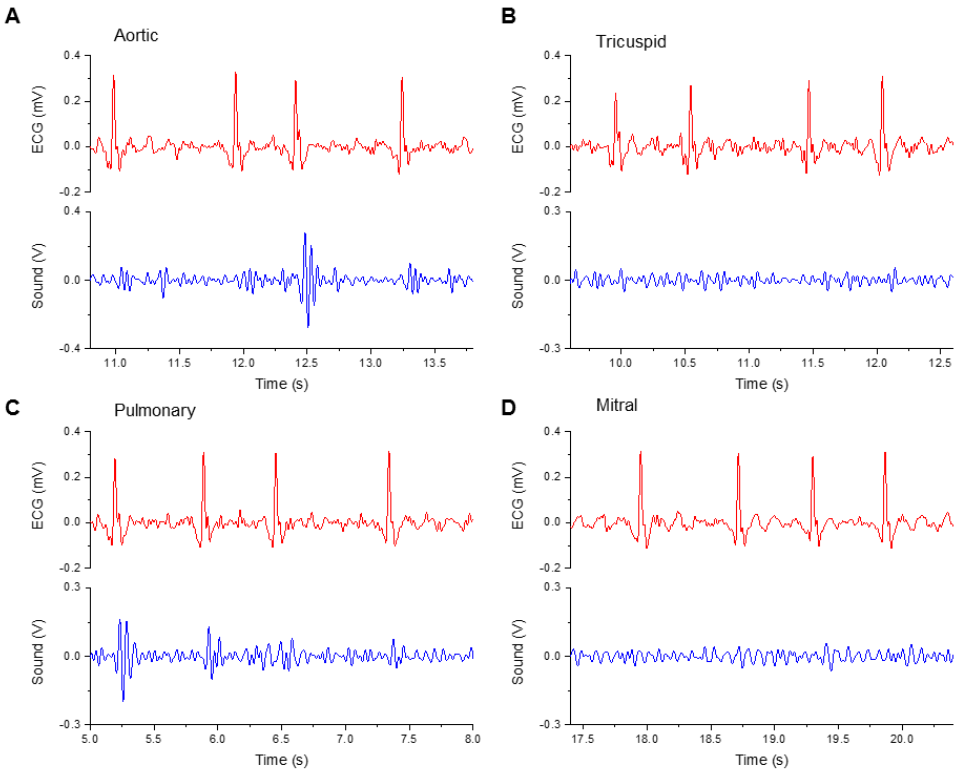

fig. S14. Acoustic signals from aortic, pulmonary, tricuspid, and mitral sites of a patient with irregular heartbeat. A representative measurement from an 82 year-old female patient with diagnosed mitral and tricuspid regurgitation at (**A**) aortic site, (**B**) tricuspid site, (**C**) pulmonary site, and (**D**) mitral site.

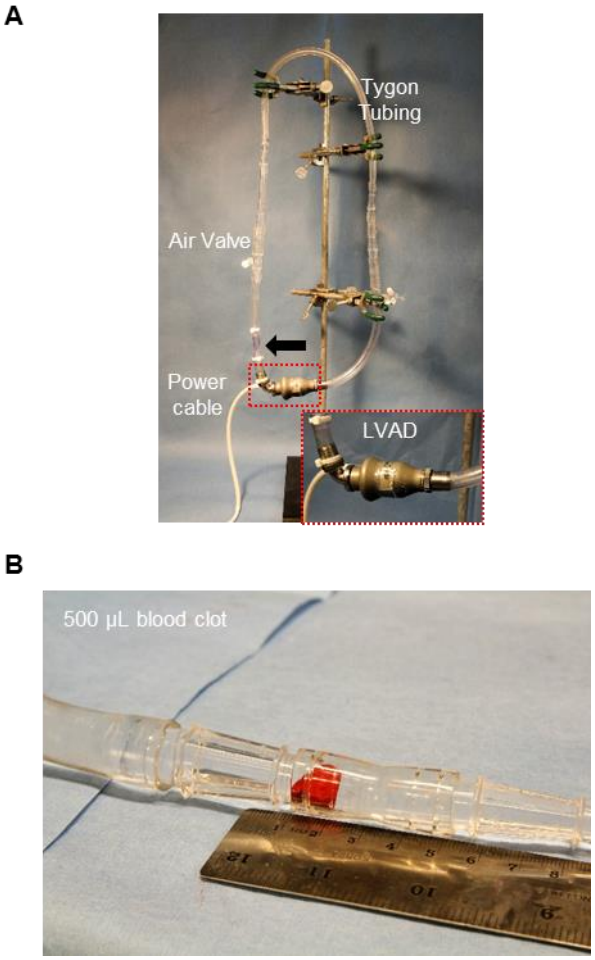

fig. S15. Experiment on LVAD pump thrombosis. (**A**) Image of a HM II LVAD device. (**B**) Image of a 500 µL blood clot injected into the circulation loop.

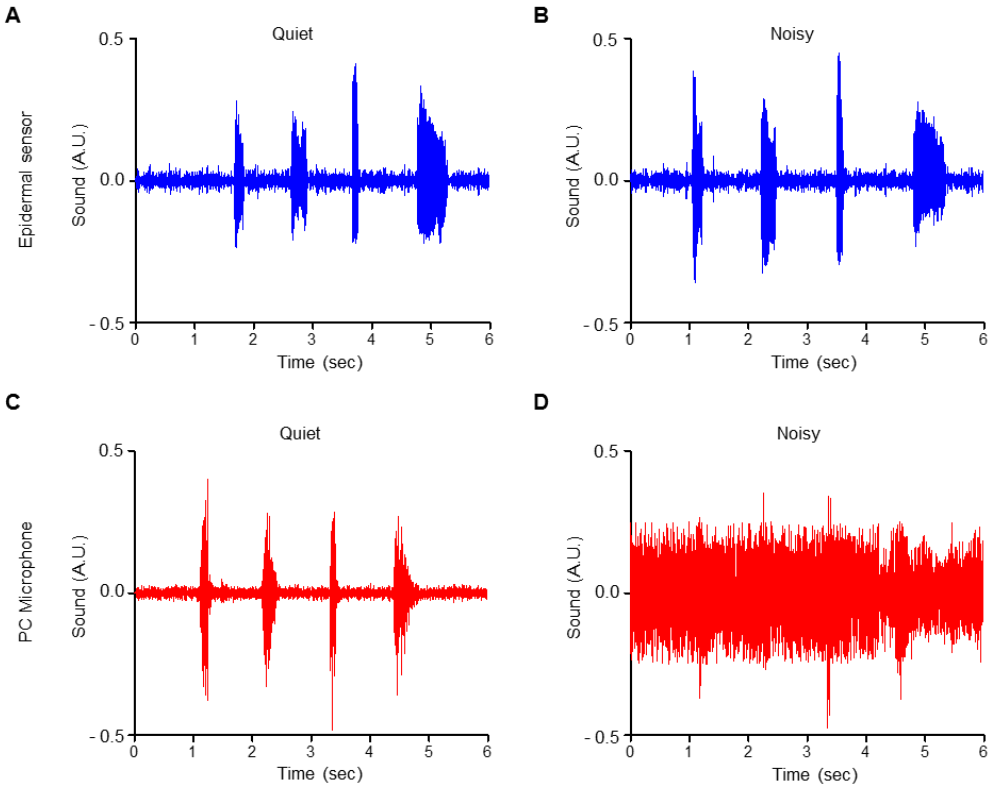

fig. S16. Data captured using a reported device and a commercial microphone in quiet and noisy environments. Data recorded in a quiet (**A**) and (**B**) noisy environment. Data recorded with a commercial microphone in a (**C**) quiet and (**D**) noisy environment.

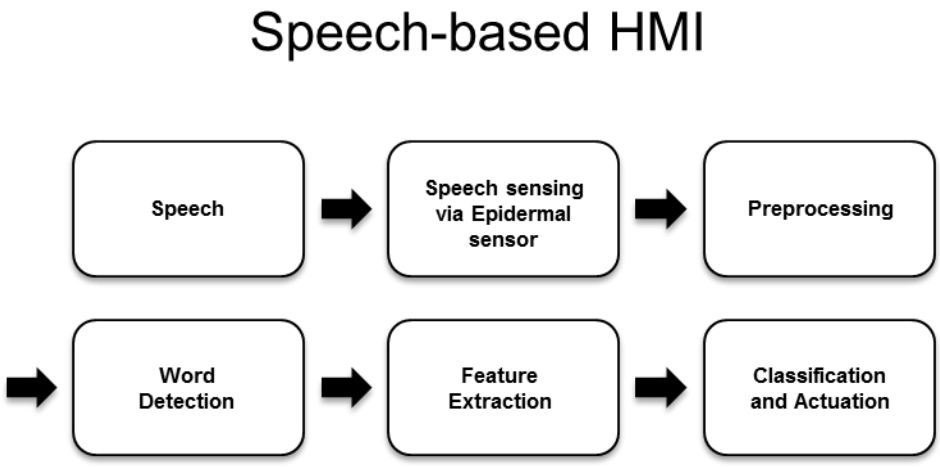

fig. S17. Process loop for a speech-based human-machine interface. Process flow of human machine interface system based on speech sensing.

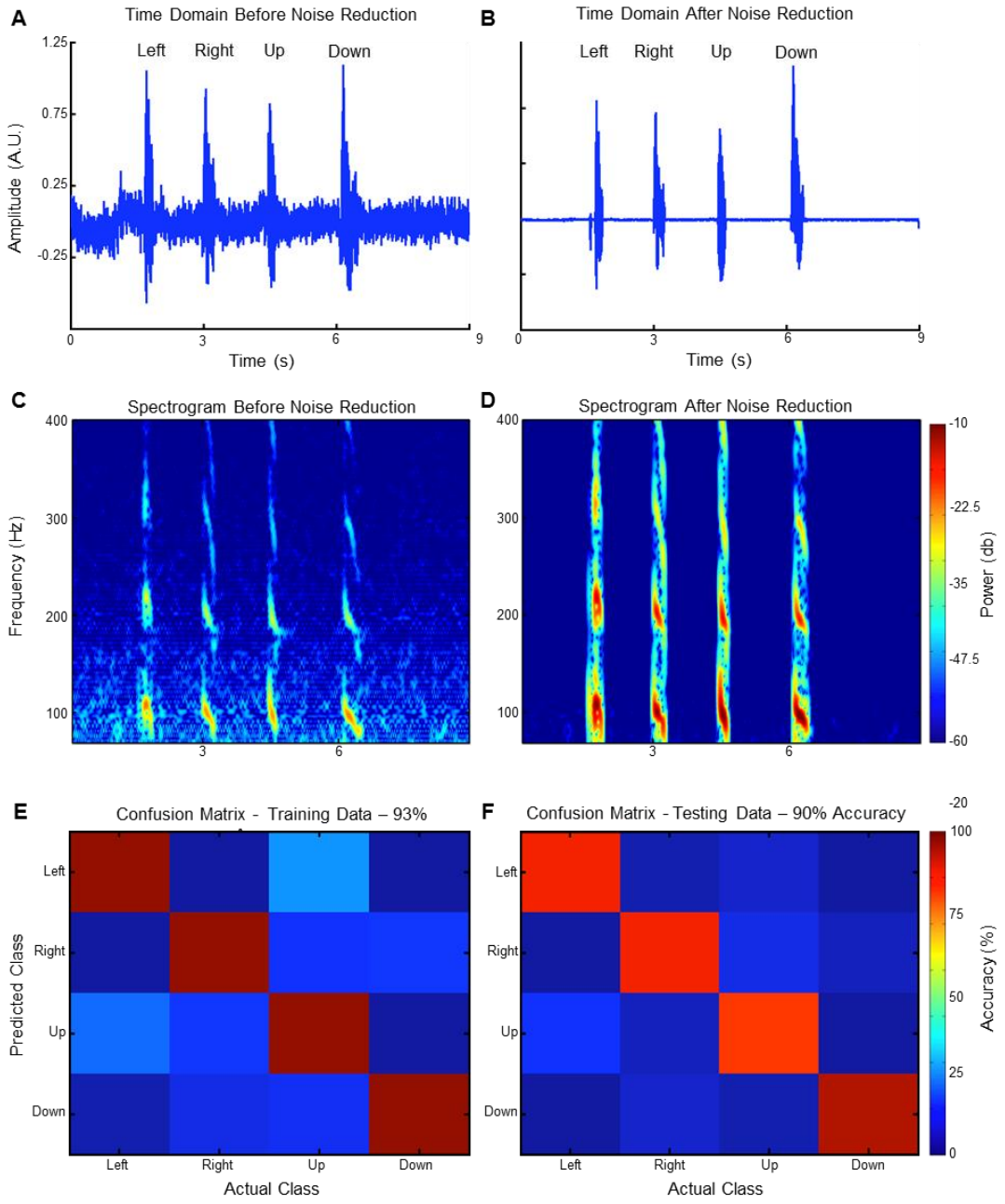

fig. S18. Demonstration of noise reduction in time domain speech data. (**A**) Speech data from the epidermal device before noise reduction. (**B**) Significant improvement in S/N ratio results from application of the noise reduction algorithm. (**C**) Spectrogram of the speech data before noise reduction, and (**D**) after noise reduction. (**E**) Confusion Matrix of the training data before noise reduction, and (**F**) after noise reduction.

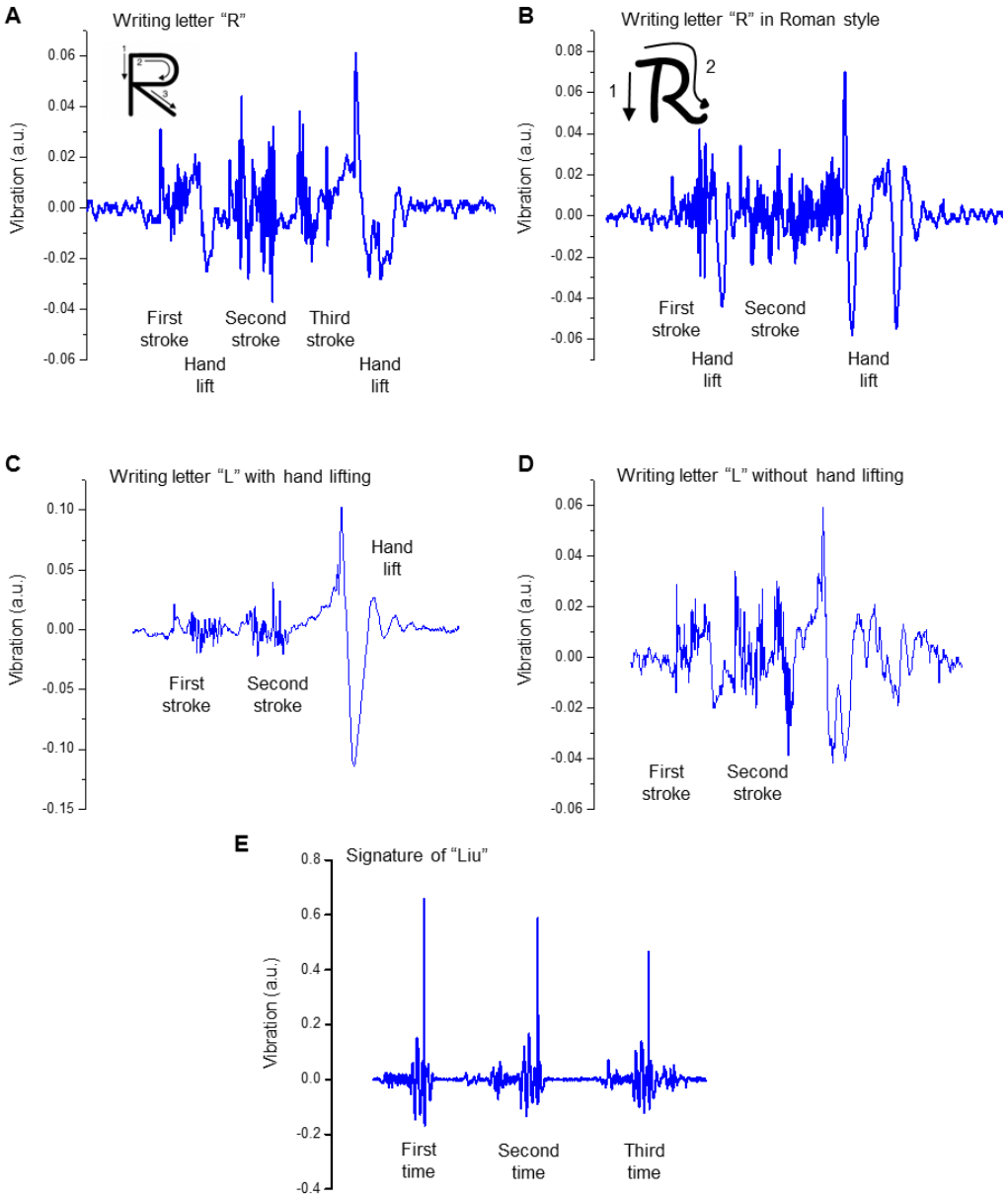

fig. S19. Authentication application. Vibration signal shows distinguishing features when writing (**A**) letter "R" in normal style, (**B**) letter "R" in Roman style, (**C**) writing "L" with hand lift, (**D**) without hand life, and (**E**) signatures.

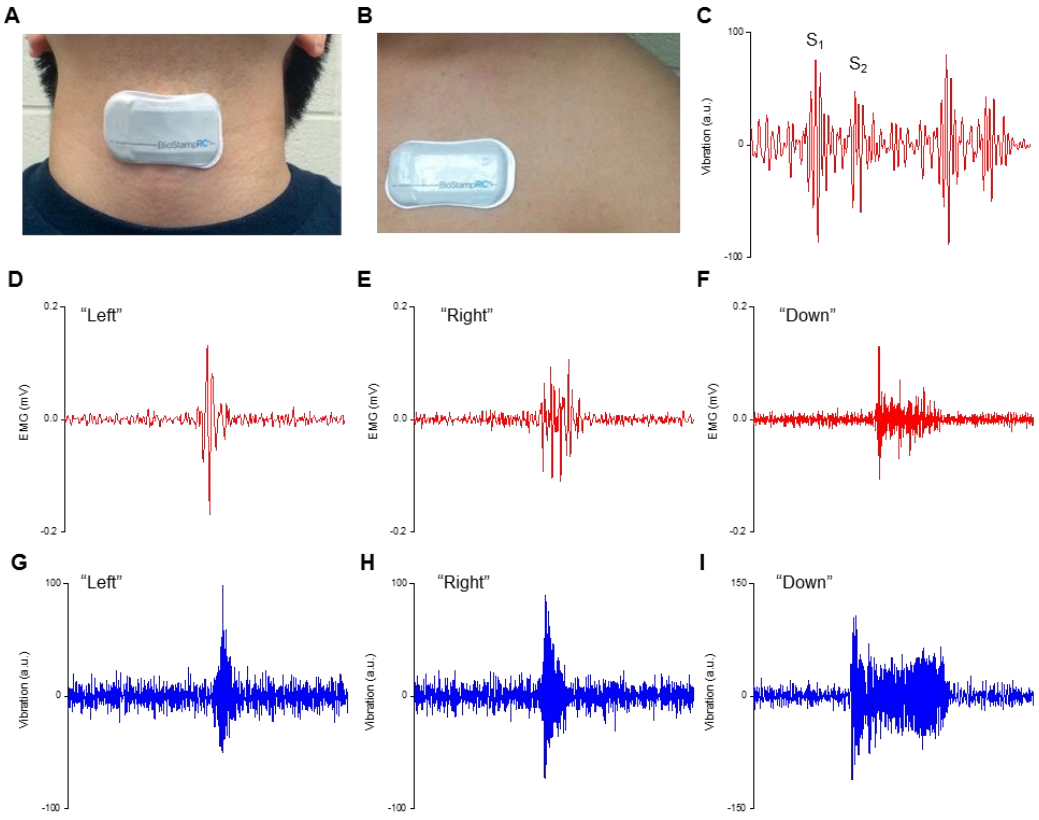

fig. S20. Wireless sensing of BioStamp. (**A**) Wireless speech sensing can be achieved by placing BioStamp on the throat surface. (**B**) Chest location for wireless heart sound sensing. (**C**) Normal heart sound (S_1 and S_2) captured by the BioStamp. Speech data in EMG acquired by the BioStamp when speaking (**D**) "Left", (**E**) "Right", and (**F**) "Down". Speech data in vibration acquired by the BioStamp when speaking (**G**) "Left", (**H**) "Right", and (**I**) "Down".

movie S1. Movie of speech recording in a quiet environment.

movie S2. Movie of speech recording in a noisy environment.

movie S3. Movie of speech recognition and voice control of a Pac-Man game with real-time machine learning and signal classification.